ROYAL SOCIETY OF CHEMISTRY

## PAPER

Check for updates

# Silver incorporated SeTe nanoparticles with enhanced photothermal and photodynamic properties for synergistic effects on anti-bacterial activity and wound healing†

Irfan Ullah, [ID] ‡[a] Shahin Shah Khan,‡[a] Waqar Ahmad,[a] Luo Liu,[a] Ahmed Rady,[b] Badr Aldahmash,[b] Changyuan Yu [ID] *[a] and Yushu Wang*[c]

Bacteria invade the host's immune system, thereby inducing serious infections. Current treatments for bacterial infections mostly rely on single modalities, which cannot completely inhibit bacteria. This study evaluates the therapeutic potential of SeTe–Ag NPs, designed with excellent photo responsiveness, with a particular focus on their dual-action antibacterial effect and wound healing properties. SeTe–Ag NPs exhibited promising synergistic antibacterial effects due to their superior photothermal and photodynamic properties. The investigation records substantial zones of inhibition of bacteria, demonstrating potent antibacterial effect. Furthermore, upon the irradiation of near-infrared (NIR) light, SeTe–Ag NPs exhibit remarkable antibiofilm and wound-healing capabilities. Overall, this study shows the applications of NIR-active SeTe–Ag NPs, which serve as a versatile platform for biomedical applications.

## 1. Introduction

The emergence of a large number of pathogenic bacteria resistant to antibiotics poses a serious concern for human health.[1-4] Furthermore, the formation of bacterial biofilms hinders drug penetration, necessitating elevated drug dosages, which can lead to adverse effects from antibiotic overdosing.[5] Therefore, a safe and effective treatment strategy is highly desired for the treatment of drug-resistant pathogens.

Photothermal therapy (PTT) and photodynamic therapy (PDT) rely on the absorption of light by photosensitizers to generate heat or reactive oxygen species (ROS) for disinfection and biofilm destruction.[6-11] However, when used independently, these methods often necessitate higher temperatures or dosages. For instance, PTT typically requires temperatures exceeding 60 °C, which can adversely affect normal tissues.[8,12] Similarly, PDT can be hindered by the hypoxic conditions within biofilms, necessitating higher dosages of photosensitizers.[13-16] Hence, combining different antibacterial

mechanisms in one system can reduce side effects and enhance antibacterial efficacy.[17-20]

The antibacterial activity of Ag NPs depends on their size. Smaller-sized NPs show better activities as compared to larger-sized NPs.[21,22] Ag NPs can reduce the duration of the wound inflammation stage and promote tissue repair and regeneration.[23-25] Furthermore, selenium (Se) and tellurium (Te) NPs have demonstrated microbicidal activities.[26] The modification of Te NPs enhances biocompatibility and confirms their therapeutic effectiveness in biological applications. Excellent nanoenzyme activity was shown by Te nanorods, which enhanced the phototherapeutic effect.[27] Bimetallic SeTe alloy NPs exhibit distinctive characteristics, exceptional photostability, and good absorbance due to their energy bandgaps, which allow them to absorb light in the visible and near-infrared regions.[28] Therefore, the combination of SeTe NPs and Ag NPs can exhibit synergistic effects against pathogenic bacteria and for wound healing.

Herein, we developed composite SeTe–Ag NPs that exhibit combined photothermal and photodynamic activity as dual-mode therapy against bacterial infection. Such a synergistic effect greatly improves antibacterial effect (Fig. 1). These NPs have photothermal and photodynamic effects, which can not only eradicate Gram-positive *Staphylococcus aureus* (*S. aureus*) and Gram-negative *Escherichia coli* (*E. coli*) by their synergetic effect but can also eradicate biofilm-associated pathogens. Furthermore, SeTe–Ag NPs also promote wound healing. Overall, SeTe–Ag NPs serve as a versatile platform to treat bacterial infections.

*aCollege of Life Science and Technology, Beijing University of Chemical Technology, No. 15 East Road of North Third Ring Road, Chao Yang District, Beijing 100029, China. E-mail: yucy@mail.buct.edu.cn*

*bDepartment of Zoology, College of Science, King Saud University, P. O. Box 2455, Riyadh 11451, Saudi Arabia*

*cSchool of Pharmaceutical Sciences, Southern Medical University, No. 1023, South Shatai Road, Guangzhou, 510515, P. R. China. E-mail: wysmjeda@gmail.com*
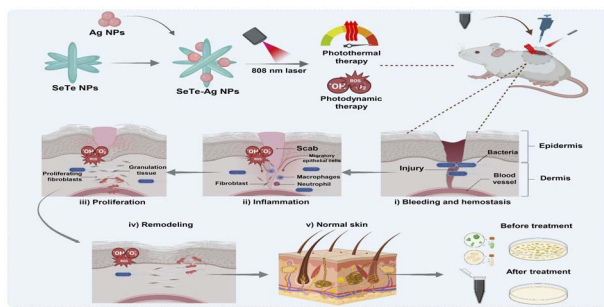
Fig. 1 Schematic illustration showing the synthesis of SeTe–Ag NPs and their antibacterial activity and wound healing mechanism using photothermal and photodynamic therapy.

## 2. Materials and methods

### 2.1. Materials and bacterial strains

All chemicals used in this work were purchased from Sigma-Aldrich, St. Louis, MO, USA., except telluric acid ($H_6TeO_6$), sodium selenite ($Na_2SeO_3$), ascorbic acid, hydrazine, cetyl-trimethylammonium bromide (CTAB), 2,2,6,6-tetramethylpi-peridine (TEMP), 5,5-dimethyl-1-pyrroline-N-oxide (DMPO), 4,6-diamidino-2-phenylindole (DAPI), 2,7-dichlorofluorescein diacetate (DCFH-DA). Ag NPs (CAS: 7440-22-4, 60–120 nm) were acquired from Shanghai Yien Chemical Technology Co., Ltd. Bacteria strains *S. aureus* (ATCC6538) and *E. coli* (ATCC8739) were obtained from China General Microbiological Culture Collection Center, Chinese Academy of Sciences.

### 2.2. Synthesis of SeTe NPs and SeTe–Ag NPs

SeTe NPs were synthesized by mixing two different reducing agents, *i.e.*, hydrazine and ascorbic acid. Briefly, sodium selenite (20 mM) and telluric acid (20 mM) were separately prepared in the presence of CTAB (2 mg mL$^{-1}$), and the final volume of the solution was raised to 100 mL. This was followed by sonication for 30 min and constant stirring in an oil bath at 250 rpm for 3 h at 95 °C. Subsequently, a mixture of two reducing agents [ascorbic acid (1 g) and hydrazine (500 μL)] prepared in 10 mL of dH$_2$O was added slowly to the above reaction and maintained for 30 min at 95 °C. Finally, a change in color appeared abruptly, from colorless to deep grey. This was followed by collection and purification of the product using centrifugation and drying overnight at 60 °C. Afterward, CTAB-mediated SeTe NPs were dissolved in dH$_2$O (0.3 g of the NPs in 30 mL) with sonication for 30 min. Subsequently, Ag NPs (2 mM in 10 mL) were mixed with sonication for 30 min and dropwise added to the as-synthesized SeTe NPs solution. The solution was stirred vigorously at 75 °C for 2 h, followed by adding 3 mL of hydrazine to reduce the free materials in the solution. Finally, SeTe–Ag NPs were collected and purified using centrifugation at 15 000 rpm for 10 minutes with 50% ethanol three times and dried overnight at 60 °C in an incubator (Fig. 2a).

### 2.3. *In vitro* anti-bacteria and antibiofilm study

The bactericidal activities of SeTe and SeTe–Ag NPs were analyzed using *S. aureus* and *E. coli* bacterial strains. Luria–Bertani (LB) broth medium was used for bacteria culture, and SeTe NPs and SeTe–Ag NPs were added in different concentrations, *i.e.*, 14, 28, 56, and 112 μg mL$^{-1}$. The bacteria and NPs mixture were irradiated with an 808 nm laser (1 W cm$^{-2}$) for 5 min. Then, the mixture was incubated for 2 h at 37 °C, followed by plating 100 μL aliquot and culturing overnight at 37 °C. To find the growth curve pattern of bacteria under the influence of NPs, bacteria with an OD of 0.4 were treated with different concentrations of NPs and cultured for 10 h, and OD$_{600}$ was recorded every hour.[29] Furthermore, for antibiofilm assay, bacterial culture of OD$_{600}$, 0.025, was added to 96 well plate and grown for 24 h at 37 °C. When the biofilms were formed on the walls, the media was removed by gently inverting the plate, and PBS was used to wash the biofilm and remove the planktonic cells. Afterward, different concentrations of SeTe NPs and SeTe–Ag NPs prepared in PBS (20, 40, 80, and 100 μg mL$^{-1}$) were added to the wells and incubated, while taking PBS treated biofilm as negative control. Then, methanol was added to fix the biofilm for 15 min and treated for 15 min with crystal violet (0.5%) prepared in PBS. Sterile PBS was used to wash the biofilm, and 33% acetic acid (v/v) was used to dissolve the crystal violet with gentle shaking for 10 min. To quantify the biofilm, the microplate reader was used to check the absorbance at 590 nm.[30]

### 2.4. Living/dead bacteria fluorescence detection

The live/dead assay was used to visualize bacterial cells. A 1.5 mL of bacterial cell culture was collected and washed with PBS, followed by treatment with 56 μg mL$^{-1}$, SeTe NPs, and SeTe–Ag NPs, and irradiated with an 808 nm laser with a power of 1 W cm$^{-2}$ for 10 minutes. After culturing the mixture for 1 h, fluorescence dye DAPI and propidium iodide (PI) were added, incubated for 15 min, and washed 3 times with PBS. For sample observation, an inverted fluorescent microscope (Leica DMI, 4000B, Danaher, Duesseldorf, Germany) was used to take photographs.

### 2.5. Intracellular ROS detection of bacteria

An intracellular ROS dye DCFH-DA (10 μM) was added to 20 mL of 0.9% NaCl solution and co-incubated for 30 min with 10$^6$ CFU mL$^{-1}$ of bacteria. Afterward, the solution was centrifuged for 5 min at 8000 rpm to remove the combined DCFH-DA. The bacterial cell treatment was performed as follows: PBS, PBS + L, SeTe–Ag NPs, SeTe–Ag NPs + L. The treatment with NIR laser (808 nm, 1 W cm$^{-2}$) lasted for 5 min and incubated for 4 h at 37 °C. The intensity of the fluorescence was recorded with a fluorometer, observed, and photographed using a confocal laser scanning microscope (CLSM).

### 2.6. SEM characterization of bacteria

The overnight-grown bacterial cells were harvested, washed three times, and incubated for 1 h with 56 μg mL$^{-1}$ of SeTe NPs and SeTe–Ag NPs for SEM analysis. All the samples were collected after irradiation with NIR laser for 10 min, centrifuged at 5000 rpm, and washed with PBS. This was followed by fixing the cells overnight with glutaraldehyde solution (2.5%) at 4 °C

and subsequently dehydrated with different concentrations of ethanol. The samples were photographed using a scanning electron microscope (SEM, Hitachi SU, 8080, Tokyo, Japan).

### 2.7. Biocompatibility evaluation

The biocompatibility of SeTe–Ag NPs was assessed using a hemolysis test. Briefly, fresh mouse blood was collected, centrifuged for 15 min at 1500 rpm to concentrate the red blood cells, and washed three times with normal saline. The concentrated red blood cells were diluted to 5% and treated with PBS, water, and different concentrations of SeTe NPs and SeTe–Ag NPs, *i.e.*, 25, 50, and 100 μg mL$^{-1}$, incubated at 37 °C for 3 h, followed by centrifugation at 11 000 rpm for 5 min. The supernatant was collected, and absorbance was recorded at 540 nm. The rate of hemolysis of SeTe–Ag NPs was calculated using PBS and water-treated groups as control.

### 2.8. Promotion of wound healing *in vivo*

All animal experiments reported in this study were conducted in accordance with the guidelines (ZYZY202209005S) and were assessed and approved by the Institutional Animal Care and Use Committee of Sino Research (Beijing) Biotechnology Co., Ltd. (China).

*In vivo* tests on wound healing were carried out on female BALB/c mice (20 ± 2 g, 5–6 weeks). All mice were subjected to skin wound creation using the reported method.[12] For the aseptic server, dorsal hairs were removed using 7% sodium sulfide and then disinfected using 75% ethanol. A round wound with a diameter of 8 mm was made on the back of each mouse using a hole puncher and infected with 10 μL of bacteria with a 10$^{-6}$ dilution factor. After 24 h, 20 μL of the synthesized NPs were added to the wounds of the corresponding groups. The synthesized NPs were applied every second day. The images of the wounds of each mouse were photographed with a camera. The wound size was calculated using ImageJ software. The wound healing rate (%) was calculated using the formula:

$$\text{Wound healing rate}(\%) = \frac{\text{area day } 0 - \text{area day } X}{\text{area day } 0} \times 100$$

area day 0 and area day *X* were the areas of the wound on day 0 and day *X*, respectively. For histological analysis, the mice were sacrificed to obtain the wound tissues to perform histological analysis on days 6 and 12. For histological observations of wounds, the skin of the wound tissue was harvested from each group and fixed in 10% formalin, followed by staining with hematoxylin and eosin (H&E).

## 3. Results and discussions

### 3.1. Characterization of SeTe–Ag NPs

**3.1.1. Morphological assessment.** The SeTe NPs with uniform shape and size were synthesized by the one-pot synthesis method at 95 °C (Fig. 2a). As depicted in Fig. 2b, TEM images revealed that SeTe NPs with sizes ranging around 150 nm and widths between 20 and 40 nm were synthesized using two reducing agents: hydrazine monohydrate and
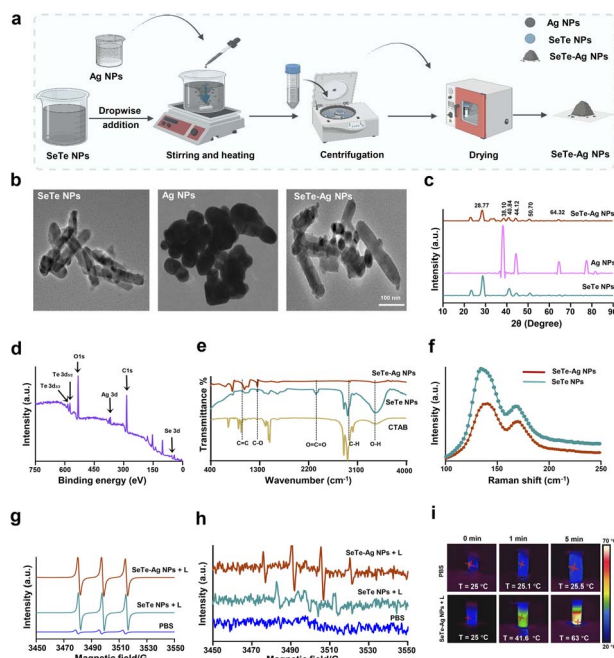


Fig. 2 Characterization of SeTe–Ag NPs. (a) A schematic illustration showing the one-pot synthesis of SeTe–Ag NPs. (b) TEM images of SeTe NPs, Ag NPs, and SeTe–Ag NPs. (c) XRD spectra of SeTe NPs, Ag NPs, and SeTe–Ag NPs. (d) Representative XPS survey spectra of SeTe–Ag NPs. (e) Fourier transform infrared (FTIR) spectra of CTAB, SeTe NPs, and SeTe–Ag NPs. (f) Raman spectra of SeTe NPs and SeTe–Ag NPs. (g) Electron paramagnetic resonance (EPR) spectra of singlet oxygen generation of SeTe NPs, SeTe–Ag NPs, and SeTe–Ag NPs + L. (h) EPR spectra of hydroxyl radical generation of SeTe NPs, SeTe–Ag NPs, and SeTe–Ag NPs + L. (i) Thermal images of heat generation by PBS and SeTe–Ag NPs under NIR irradiation for five minutes.

ascorbic acid.[29] Further, Ag NPs of 60–120 nm size have been physically immobilized on the SeTe NPs surface at 75 °C for 2 h to synthesize SeTe–Ag NPs. Notably, Ag NPs can be observed on the surface of SeTe NPs. Furthermore, the basic spectral outline of NPs obtained by EDS showing the metalloid amalgamation was confirmed by high-resolution mapping. EDS spectra show all the elements of Se, Te, and Ag (Fig. S1†), which support the synthesis of SeTe–Ag NPs.[29]

**3.1.2. X-ray crystallography.** The incorporated SeTe NPs retain their respective crystallinity as determined by the XRD pattern, and the corresponding diffraction bands well matched the diffraction profile of the chalcogenide family (Fig. 2c). As Se and Te are perfectly isomorphous, they can develop a solid mass in which the Se and Te atoms are arbitrarily distributed alongside the helical chain connected *via* covalent bonding, and the chains are in turn linked together by van der Waals forces, thus creating a hexagonal array. The prominent diffraction peak at $2\theta = 28.77°$ shows that CTAB directs the growth of SeTe NPs in the (101) lattice plane reference.[29] Furthermore, Ag NPs were incorporated on the surface of SeTe NPs. The typical face-centered cubic crystal structures of the Ag NPs are reflected at 38.1° (111), 44.1° (200), 64.3° (220), and 77.2° (311), as compared to Ag NPs.

**3.1.3. X-ray photoelectron spectroscopy (XPS).** The binding energies of SeTe NPs and SeTe–Ag NPs were studied using X-ray photoelectron spectroscopy (XPS). The spectrum of composite NPs confirmed the individual elements, Se, Te, O, and Ag (Fig. 2d). The binding energy of each component was analyzed for SeTe–Ag NPs, and each spectrum is shown in Fig. S2†. This confirms the presence of Ag NPs on the surface of bimetallic SeTe NPs. The two major peaks were deconvoluted for Ag 3d containing Ag $3d_{5/2}$ on 365 eV while Ag $3d_{3/2}$ was observed on 374 eV. Deconvoluted Te 3d spectra show four different spectral bands at binding energies of 572.8, 575.8, 583.4, and 586.3 eV. The peaks obtained at 583.4 and 572.8 eV correspond to $3d_{3/2}$ and $3d_{5/2}$ of Te (0) 3d, while the other two bands correspond to Te(IV) 3d, as depicted in Fig. S2†. The co-existence of the two forms indicates that Te exists in both the elemental and oxide forms. Furthermore, Fig. S2† shows Se 3d spectra having two different bands at 55.1 eV (Se $3d_{3/2}$) and 54.2 eV (Se $3d_{5/2}$), while a broad band observed around 60.2 eV is assigned to the $SeO_2$ bond in SeTe–Ag NPs.[29]

**3.1.4. Fourier-transform infrared spectroscopy.** FTIR analysis was carried out (Fig. 2e). The peak at 3426.88 $cm^{-1}$ represents the OH stretch in all CTAB, SeTe NPs, and SeTe–Ag NPs while 1627.62 $cm^{-1}$ represents the stretching of C=O.[31] The band at 1045.21 $cm^{-1}$ belongs to the C–O–C stretching vibration of the alkoxy group in SeTe NPs, where a slight shifting occurs to 1085 $cm^{-1}$ in SeTe–Ag NPs, thus suggesting the presence of Ag NPs on the surface of CTAB mediated SeTe NPs.[32] The IR band at 2337.30 $cm^{-1}$ corresponds to the $CO_2$ vibration line in SeTe NPs, while in SeTe–Ag NPs, it shifted to 2339 $cm^{-1}$, a very negligible peak. The symmetrical and asymmetrical stretching vibrations of the methylene group of aliphatic compounds were responsible for the two prominent bands at 2959 $cm^{-1}$ and 2840 $cm^{-1}$, respectively.[33]

**3.1.5. Raman-spectroscopy.** The structural connection between SeTe–Ag NPs and CTAB-mediated SeTe NPs is shown by Raman-spectroscopic investigation (Fig. 2f). The presence of Ag NPs is indicated by the shift in peak intensity and position when compared to the SeTe NPs alone. This peak shift, particularly noticeable around 140 $cm^{-1}$ and 180 $cm^{-1}$, indicates the interaction between Ag NPs and the SeTe NPs matrix, potentially altering the vibrational modes of the NPs. These modifications suggest that doping SeTe NPs with Ag NPs not only affects their optical properties but may also influence their chemical reactivity and physical stability.

## 3.2. Photodynamic and photothermal analysis

**3.2.1. Photodynamic assessment.** EPR analysis was used to study the ROS generation. NIR laser (1 W $cm^{-2}$, 1–5 minutes) was applied to SeTe NPs and SeTe–Ag NPs. TEMP and DMPO were used to check the release of singlet oxygen and OH radicals. The TEMP is a common trapping agent for singlet oxygen generation detection and was used for SeTe NPs and SeTe–Ag NPs. The reaction of $^1O_2$ with TEMP produced the TEMPO adduct. The EPR spectra of SeTe NPs and SeTe–Ag NPs are shown in Fig. 2g for singlet oxygen generation. Furthermore, a hydroxyl radical trapping agent, 5,5-Dimethyl-1-Pyrroline-*N*-

Oxide (DMPO), was used for synthesized SeTe NPs and SeTe–Ag NPs (Fig. 2h), same as for TEMP. The samples were irradiated with NIR laser for 1–5 minutes, and prominent signals of hydroxyl radicals were recorded by EPR. The successful production of singlet oxygen and hydroxyl ions by SeTe NPs and SeTe–Ag NPs in the presence of NIR laser can be attributed to surface-capped proteins and open oxygen vacancies in the NIR region. The excitation of electrons in samples treated with NIR laser could accelerate the soluble oxygen for ROS production. The literature shows that NPs that incorporate biologically capped moieties, such as (β-hydroxypropyl-cyclodextrin), could synergistically enhance the production of ROS as compared to free NPs.[34]

**3.2.2. Photothermal performance.** The photothermal performance of the resulting SeTe NPs and SeTe–Ag NPs was measured under 808 nm laser irradiation (1 W $cm^{-2}$). The temperature showed a concentration-dependent increase pattern. The temperature of the solution (96 μg $mL^{-1}$) increased to 63 °C within 5 minutes, while the recorded temperature of SeTe NPs reached 48 °C as compared to the PBS, which was 25.5 °C; the corresponding photothermal images are shown in Fig. 2i and S3c.† The photothermal stability of SeTe–Ag NPs was measured by irradiating with 808 nm laser (1 W $cm^{-2}$) for 5 min (laser on) and then switching off the laser to cool naturally to room temperature (laser off) for 5 min, and this was repeated for a total of 5 cycles (Fig. S3b†). The photothermal effect of the SeTe–Ag NPs solution had a negligible change, and a slight deterioration was observed during five laser on/off cycles, proving the excellent photothermal stability of SeTe–Ag NPs.[35] Furthermore, a single cycle of SeTe–Ag NPs heating/cooling processes under NIR laser irradiation is provided in Fig. S3a,† which proves the excellent photothermal stability of SeTe–Ag NPs.[36] These results indicate that the photothermal properties of SeTe NPs could be improved by the incorporation of Ag NPs.

## 3.3. Enhanced antibacterial and antibiofilm activity

**3.3.1. Zones of inhibition.** As bactericidal activity is directly proportional to the zone of inhibition assay, it was used to assess the bactericidal activity of SeTe–Ag NPs. As expected, SeTe–Ag NPs treatment showed extremely high bactericidal activity against both *S. aureus* and *E. coli*. The diameter of the zone of inhibition of SeTe–Ag NPs against *S. aureus* and *E. coli* were 34 ± 1 mm and 33 ± 1 mm, respectively. The diameter of zones of inhibition was recorded differently for the samples treated with SeTe NPs, Ag NPs, and SeTe–Ag NPs. The data obtained clearly shows that SeTe–Ag NPs have enhanced bactericidal activity against both Gram-negative and Gram-positive strains in comparison with its individual components (Fig. S4†).

**3.3.2. Antibiofilm activity.** Furthermore, since biofilm can be formed by many bacteria, especially in chronic wounds, the antibiofilm activity of the as-synthesized SeTe–Ag NPs against *E. coli* and *S. aureus* was evaluated. Biofilm was grown in a static condition in the presence of as-synthesized NPs. The formation of biofilm was assessed by staining the biofilm with crystal violet. A reduction in biofilm mass of the tested bacterial strains was caused by synthesized NPs, as shown in Fig. 3a and b,
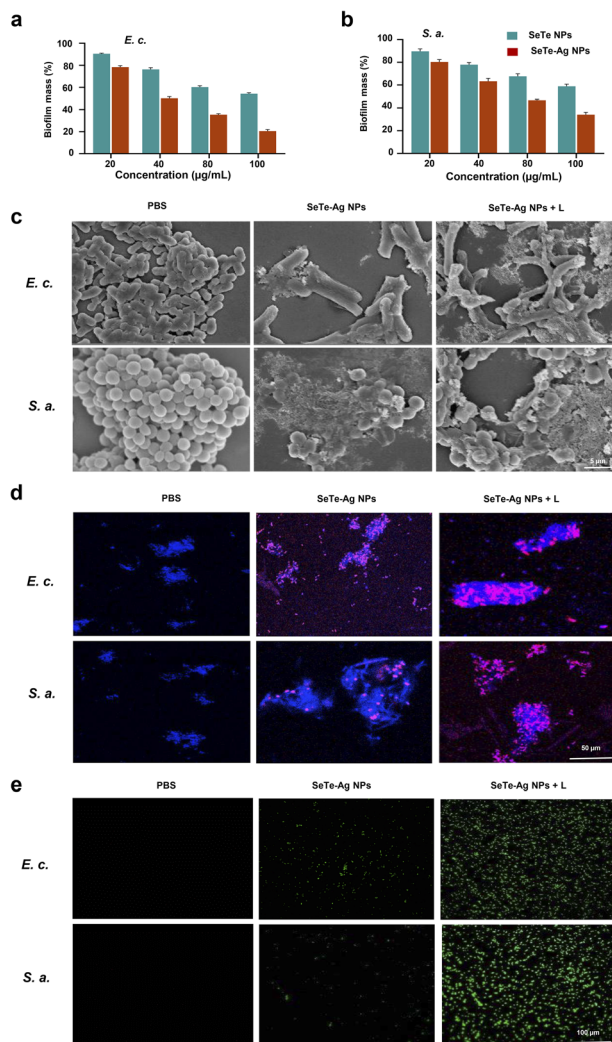
Fig. 3 Antibacterial activities of SeTe–Ag NPs. (a and b) Antibiofilm activity of SeTe NPs and SeTe–Ag NPs against *E. coli* and *S. aureus*. (c) SEM images of bacteria treated with PBS, SeTe–Ag NPs, and SeTe–Ag NPs + L. (d) CLSM images of live/dead bacteria after treatment with PBS, SeTe–Ag NPs, and SeTe–Ag NPs + L. (e) Fluorescence micros-copy images of intracellular ROS generation of bacteria treated with PBS, SeTe–Ag NPs, and SeTe–Ag NPs + L.

exhibiting excellent antibiofilm activity against both Gram-positive and Gram-negative bacterial strains.[37] After biofilm inhibition, the growth curve study was also evaluated to investigate the effect of synthesized NPs.

**3.3.3. Bacterial growth patterns.** The growth patterns of bacteria treated with different concentrations of the NPs show that the growth of bacteria were inhibited under all tested concentrations (Fig. S5†). The untreated bacteria grow normally and reach the stationary phase after 24 h. On the other hand, *E. coli*, and *S. aureus* bacteria were completely inhibited at 14, 28, 56, and 112 $\mu$g mL$^{-1}$ concentrations of SeTe–Ag NPs. The results show that the bactericidal activity of NPs increased with an increase in concentration.[29]

**3.3.4. Agar plate method.** The agar plate method was used to investigate the effect of NPs on the growth of bacteria, with and without using NIR laser irradiation (Fig. S6†). The results

obtained showed that SeTe–Ag NPs are very active against both bacterial strains. Promising results were exhibited by SeTe–Ag NPs when applied with NIR laser irradiation.

**3.3.5. Membrane disruption study.** Further, to confirm the antibacterial activity of the synthesized NPs, bacterial cell cultures with different concentrations of NPs were used to study the membrane disruption. The SEM images of untreated *S. aureus* cells showed a typical spherical shape with an intact and smooth surface and *E. coli* with a rod shape. However, the differential changes could be caused by all the nanomaterials on the cell surface of bacteria. Moreover, the as-synthesized SeTe–Ag NPs could result in membrane damage, enhancing the permeability of SeTe–Ag NPs, which enhances the efficiency of killing bacteria (Fig. 3c).[29,38]

**3.3.6. Live/dead assay.** Finally, live/dead staining DAPI and PI probes[39,40] were used to assess the bactericidal effect of SeTe–Ag NPs. As shown in Fig. 3d, bacteria treated with PBS emitted blue fluorescence, indicating the presence of living bacteria. The group treated with SeTe–Ag NPs shows that more than half of the bacterial cells emitted red fluorescence, which indicates the presence of dead bacteria. Moreover, the ratio of live/dead bacteria in the SeTe–Ag NPs + L treated group was signifi-cantly higher. These results indicate that the synthesized nanoparticles have the strongest bactericidal activity due to the combined effect of SeTe NPs with Ag NPs.[41,42]

### 3.4. Antibacterial mechanism

There is a close association of oxidative stress with the bacte-ricidal process of Ag NPs.[43] ROS is involved in pathological and physiological processes, including apoptosis.[44] It is reported that the activity of Ag NPs with a size below 10 nm is because of the nanoparticles themselves. In fact, the small-sized Ag NPs adhere to the bacterial surface, altering the permeability and entering inside the bacteria, causing damage to various targets. However, for large-size NPs, the silver ion release is the main mechanism. Various studies reported that silver ions kill bacteria by up-regulating ROS levels.[45,46] Therefore, the change in ROS level by SeTe NPs, SeTe–Ag NPs, and SeTe–Ag NPs + L was evaluated, as shown in Fig. 3e, and the corresponding fluorescence activities are mentioned in Fig. S7.† The green fluorescence increased gradually in the order of SeTe NPs, SeTe–Ag NPs, and SeTe–Ag NPs + L, showing an increase in ROS production. Furthermore, these results confirm inducing hydroxyl radicals by SeTe–Ag NPs + L. Due to the production of basal level of ROS as a respiratory product by cells, the Ag (0) can be oxidized to Ag$^+$, which further increases the production of ROS to damage the subcellular components.[47] The induced oxidative stress of the cell is likely responsible for bacterial apoptosis, and the higher level of ROS can affect the function and activity of the bacterial biomacromolecules. From these results, it is clear that the bactericidal effect of SeTe–Ag NPs was due to the induced production of ROS.

### 3.5. *In vivo* antibacterial activity and wound healing

**3.5.1. Cytotoxicity assessment.** Before it can be used for wound healing, cytotoxicity and biocompatibility of the as-

synthesized NPs were analyzed using hemolysis.[48] As depicted in Fig. S8,† non-hemolytic rates of samples treated with different concentrations of nanomaterials were lower than 5%, which shows that SeTe NPs and SeTe–Ag NPs did not cause hemolysis.

**3.5.2. Wound healing study.** In the current study, an infected wound model was constructed by injecting the test bacteria into the wounds on the back of BALB/c mice (6–8 weeks),[49,50] as depicted in the schematic diagram in Fig. 4a. A total of four groups (each group with 5 mice) were made on the basis of different treatments. After injecting bacteria, severe infection was exhibited by all mice. After 24 h of infection, the infected wounds were treated with SeTe NPs, SeTe–Ag NPs, and SeTe–Ag NPs + L every second day. The mice treated with SeTe NPs and SeTe–Ag NPs showed a wound closure of 52.8% and 68%, respectively. After treatment for 12 days, the SeTe–Ag + L treated wound area sharply decreased with a wound closure of 96.3%, which is higher than the PBS treatment group (Fig. 4b

and S9†). These results show that the combined effect of SeTe–Ag NPs and NIR light improved the bactericidal activity against *E. coli* and *S. aureus* and significantly improved wound healing as compared to other single-mode therapies. Additionally, all the treated groups did not show any significant difference in body weight, as shown in Fig. S10,† which shows the biosafety of the NPs in mice.

**3.5.3. Hematoxylin and eosin staining.** The major steps involved in the wound healing process are the formation of granulation tissues and re-epithelialization,[51] which was characterized by H&E staining, while Giemsa staining was used for the investigation of any test bacteria residue in wound tissues. In the PBS treatment group, a large number of inflammatory cells were observed. While the groups treated with SeTe NPs, SeTe–Ag NPs, and SeTe–Ag NPs + L show an intact layer of the epidermis, a circular layer as well as a smaller number of inflammatory cells were emerged on the wound (Fig. 4c). Meanwhile, on day 12 in all of the treated groups, elongated epithelial and fibroblasts were observed. Among all the treated groups, hair follicle development and thicker granulation tissue appeared in the SeTe–Ag NPs + L treated group, which shows the significant healing efficiency of the as-synthesized NPs. When the wounds were infected with the test bacteria (*E. coli* and *S. aureus*), the sections of the skin tissues collected after treatment with NPs were the same as before, except that the granulation tissue thickness in the process of skin healing of SeTe–Ag NPs and SeTe–Ag NPs + L treated groups were basically the same.

**3.5.4. Giemsa staining.** Giemsa staining of the collected tissues on day 6 and day 12 was also performed. As indicated in Fig. 4d, a significant number of bacteria can be seen in the PBS, SeTe NPs, and SeTe–Ag NPs treatment groups on day 6. On the other hand, as compared to the PBS group, there was a lower number of bacterial residues or infections seen in SeTe NPs, followed by the SeTe–Ag NPs treatment group on day 12. In contrast, there were no detectable signs of infection or bacteria in the SeTe–Ag NPs + L treatment group. These results show that SeTe–Ag NPs have a strong antibacterial activity when applied with NIR laser irradiation, which confirms the *in vitro* antibacterial activity.

**3.5.5. Wound bacteria quantification.** The wound tissue was excised to quantify the number of bacteria in these wounds, which shows the bactericidal efficiency of the as-synthesized NPs. The results obtained from the standard agar plate dilution assay show that SeTe–Ag NPs + L have higher bactericidal activity, which is obvious from the small number of bacterial colonies, compared to other groups (Fig. S11†).

# 4. Conclusions

In this study, hybrid NPs were synthesized using the one-pot synthesis method for combating both the Gram-positive and Gram-negative bacterial strains. The results reveal that appropriately combining the NPs with NIR laser enhances the therapeutic efficacy compared to the individual components of the NPs. In comparison with the bactericidal efficiency of Ag NPs alone, the composite NPs showed a pronounced and combinational bactericidal effect. Furthermore, the synthesized SeTe–
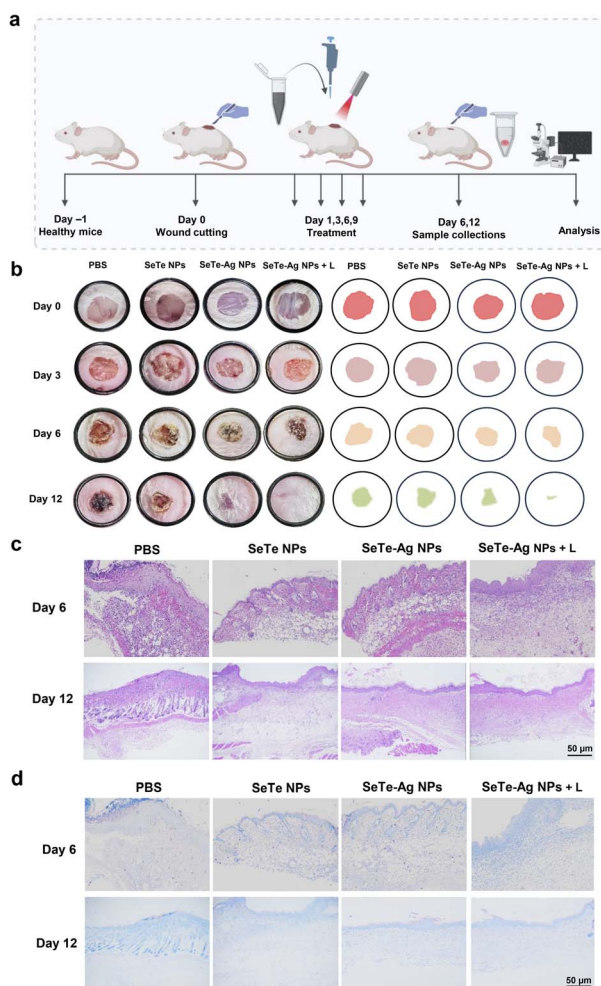


**Fig. 4** *In vivo* evaluation of SeTe–Ag NPs. (a) Schematic illustration of *in vivo* study. (b) Wound healing images at different times (day 0, 3, 6, and 12) after treatment with PBS, SeTe NPs, SeTe–Ag NPs, and SeTe–Ag NPs + L. (c) H&E staining of wound tissues of PBS, SeTe NPs, SeTe–Ag NPs and SeTe–Ag NPs + L, treatment groups on day 6 and day 12. (d) Giemsa staining of wound tissues of PBS, SeTe NPs, SeTe–Ag NPs and SeTe–Ag NPs + L treatment groups on day 6 and day 12.

Ag NPs exhibited higher stability and good biocompatibility. The mechanism of activity exploration of the combination bactericidal strategy shows that the designed nanomaterial disturbs cell integrity, generating ROS and damaging the cell membrane of bacteria. *In vivo* studies showed improved wound healing in mice. Overall, synergistic activities using dual or multiple nanomaterials could significantly reduce the dosage required for traditional antibiotics, reduce toxicity effects, and screen effective candidates for the treatment of drug-resistant bacterial infections.

## Author contributions

Irfan Ullah: experimental work, writing the original draft. Shahin Shah Khan: conceptualization, experimental work, data analysis, and reviewing the draft. Waqar Ahmad: formal analysis, Liu Luo: conceptualization, draft modification. Ahmed Rady: conceptualization, Badr Aldahmash: conceptualization, Changyuan Yu: conceptualization, supervision, and reviewing the draft. Yushu Wang: conceptualization, reviewing the draft.

## Conflicts of interest

There are no conflicts to declare.

## Acknowledgements

## References

1 C. J. Murray, K. S. Ikuta, F. Sharara, L. Swetschinski, G. R. Aguilar, A. Gray, C. Han, C. Bisignano, P. Rao and E. Wool, *Lancet*, 2022, **399**, 629–655.
2 Z. Wang, B. Koirala, Y. Hernandez, M. Zimmerman, S. Park, D. S. Perlin and S. F. Brady, *Nature*, 2022, **601**, 606–611.
3 Y. Yu, F. Bu, H. Zhou, Y. Wang, J. Cui, X. Wang, G. Nie and H. Xiao, *Mater. Chem. Front.*, 2020, **4**, 1930–1953.
4 J. Zhang, H. Guo, M. Liu, K. Tang, S. Li, Q. Fang, H. Du, X. Zhou, X. Lin and Y. Yang, *Exploration*, 2023, 20230087.
5 M. Berditsch, S. Afonin, J. Reuster, H. Lux, K. Schkolin, O. Babii, D. S. Radchenko, I. Abdullah, N. William and V. Middel, *Sci. Rep.*, 2019, **9**, 17938.
6 Y. Wang, H. Yao, Y. Zu and W. Yin, *RSC Adv.*, 2022, **12**, 8862–8877.
7 Y. Zhao, P. He, J. Yao, M. Li, B. Wang, L. Han, Z. Huang, C. Guo, J. Bai and F. Xue, *Biomaterials*, 2023, **301**, 122237.
8 H. Zhou, D. Tang, X. Kang, H. Yuan, Y. Yu, X. Xiong, N. Wu, F. Chen, X. Wang and H. Xiao, *Adv. Sci.*, 2022, **9**, 2200732.
9 Y. Yu, D. Tang, C. Liu, Q. Zhang, L. Tang, Y. Lu and H. Xiao, *Adv. Mater.*, 2022, **34**, 2105976.
10 L. Wang, Y. Yu, D. Wei, L. Zhang, X. Zhang, G. Zhang, D. Ding, H. Xiao and D. Zhang, *Adv. Mater.*, 2021, **33**, 2100599.
11 M. Shen, Y. Wang, T. Bing, Y. Tang, X. Liu and Y. Yu, *Adv. Funct. Mater.*, 2023, **33**, 2307013.
12 H. L. Zhou, D. S. Tang, X. X. Kang, H. T. Yuan, Y. J. Yu, X. L. Xiong, N. E. Wu, F. Z. Chen, X. Wang, H. H. Xiao and D. S. Zhou, *Adv. Sci.*, 2022, **9**, 2200732.
13 H. X. Zhang, Y. Zou, K. Y. Lu, Y. Wu, Y. C. Lin, J. J. Cheng, C. X. Liu, H. Chen, Y. X. Zhang and Q. Yu, *J. Mater. Sci. Technol.*, 2024, **169**, 209–219.
14 T. Du, Z. Xiao, G. Zhang, L. Wei, J. Cao, Z. Zhang, X. Li, Z. Song, W. Wang and J. Liu, *Acta Biomater.*, 2023, **161**, 112–133.
15 M. Qi, X. Ren, W. Li, Y. Sun, X. Sun, C. Li, S. Yu, L. Xu, Y. Zhou and S. Song, *Nano Today*, 2022, **43**, 101447.
16 H. He, L. Du, H. Xue, J. Wu and X. Shuai, *Acta Biomater.*, 2022, **149**, 297–306.
17 J. Lv, Y. Qi, Y. Tian, G. Wang, L. Shi, G. Ning and J. Ye, *Biomater. Sci.*, 2022, **10**, 3747–3756.
18 Y. Zhang, X.-F. Qu, C.-L. Zhu, H.-J. Yang, C.-H. Lu, W.-L. Wang, Y. Pang, C. Yang, L.-J. Chen and X.-F. Li, *ACS Appl. Bio Mater.*, 2021, **4**, 4821–4832.
19 G. Xiong, D. Huang, L. Lu, X. Luo, Y. Wang, S. Liu, M. Chen, S. Yu, M. Kappen and C. You, *Small Methods*, 2022, **6**, 2200379.
20 B. Yu, Y. Wang, T. Bing, Y. Tang, J. Huang, H. Xiao, C. Liu and Y. Yu, *Adv. Mater.*, 2024, **36**, 2310456.
21 Y. Zhao, Z. Zhang, Z. Pan and Y. Liu, *Exploration*, 2021, **1**, 20210089.
22 S. Li, Y. Yang, S. Wang, Y. Gao, Z. Song, L. Chen and Z. Chen, *Exploration*, 2022, **2**, 20210223.
23 S. Skanda, P. Bharadwaj, V. D. Darshan, V. Sivaramakrishnan and B. Vijayakumar, *J. Microbiol. Methods*, 2022, **199**, 106517.
24 S. Wu, A. Li, X. Zhao, C. Zhang, B. Yu, N. Zhao and F.-J. Xu, *ACS Appl. Mater. Interfaces*, 2019, **11**, 17177–17183.
25 J. Ma and C. Wu, *Exploration*, 2022, **2**, 20210083.
26 W. Pan, C. Liu, Y. Li, Y. Yang, W. Li, C. Feng and L. Li, *Bioact. Mater.*, 2022, **13**, 96–104.
27 S. Kang, Y.-G. Gil, D.-H. Min and H. Jang, *ACS Nano*, 2020, **14**, 4383–4394.
28 L. D. Geoffrion and G. Guisbiers, *Nanoscale Adv.*, 2021, **3**, 4254–4270.
29 S. S. Khan, I. Ullah, S. Zada, A. Ahmad, W. Ahmad, H. Xu, S. Ullah and L. Liu, *Materials*, 2022, **15**, 4813.
30 Y. Yu, Y. Zhang, Y. Cheng, Y. Wang, Z. Chen, H. Sun, X. Wei, Z. Ma, J. Li and Y. Bai, *Bioact. Mater.*, 2022, **13**, 269–285.
31 N. Alfryyan, M. G. Kordy, M. Abdel-Gabbar, H. A. Soliman and M. Shaban, *Sci. Rep.*, 2022, **12**, 12495.
32 S. Ullah, A. Ahmad, F. Subhan, A. Jan, M. Raza, A. U. Khan, A.-U. Rahman, U. A. Khan, M. Tariq and Q. Yuan, *J. Photochem. Photobiol., B*, 2018, **183**, 342–348.
33 A. Negash, S. Mohammed, H. D. Weldekirstos, A. D. Ambaye and M. Gashu, *Sci. Rep.*, 2023, **13**, 22234.

34 G. Vasiliev, A.-L. Kubo, H. Vija, A. Kahru, D. Bondar, Y. Karpichev and O. Bondarenko, *Sci. Rep.*, 2023, **13**, 9202.

35 S. Zada, W. Dai, Z. Kai, H. Lu, X. Meng, Y. Zhang, Y. Cheng, F. Yan, P. Fu and X. Zhang, *Angew. Chem., Int. Ed.*, 2020, **59**, 6601–6606.

36 Z. Liu, Z. Liu, Z. Zhao, D. Li, P. Zhang, Y. Zhang, X. Liu, X. Ding and Y. Xu, *Nanomaterials*, 2022, **12**, 2469.

37 O. Tarawneh, H. Abu Mahfouz, L. Hamadneh, A. A. Deeb, I. Al-Sheikh, W. Alwahsh and A. Fadhil Abed, *Sci. Rep.*, 2022, **12**, 3900.

38 D. P. Linklater, V. A. Baulin, X. Le Guével, J. B. Fleury, E. Hanssen, T. H. P. Nguyen, S. Juodkazis, G. Bryant, R. J. Crawford and P. Stoodley, *Adv. Mater.*, 2020, **32**, 2005679.

39 Y. Yu, R. Tian, Y. Zhao, X. Qin, L. Hu, J. J. Zou, Y. W. Yang and J. Tian, *Adv. Healthcare Mater.*, 2023, **12**, 2201651.

40 Y. Yu, D. Wei, T. Bing, Y. Wang, C. Liu and H. Xiao, *Adv. Mater.*, 2024, DOI: **10.1002/adma.202402452**.

41 Z. Li, S. Lu, W. Liu, T. Dai, J. Ke, X. Li, R. Li, Y. Zhang, Z. Chen and X. Chen, *Angew. Chem., Int. Ed.*, 2021, **60**, 19201–19206.

42 Z. Liu, X. Zhao, B. Yu, N. Zhao, C. Zhang and F.-J. Xu, *ACS Nano*, 2021, **15**, 7482–7490.

43 G. Fang, W. Li, X. Shen, J. M. Perez-Aguilar, Y. Chong, X. Gao, Z. Chai, C. Chen, C. Ge and R. Zhou, *Nat. Commun.*, 2018, **9**, 129.

44 X. Bi, Q. Bai, M. Liang, D. Yang, S. Li, L. Wang, J. Liu, W. W. Yu, N. Sui and Z. Zhu, *Small*, 2022, **18**, 2104160.

45 P.-P. Li, Y. Zhang, C. Wang, S.-J. Wang, W.-Q. Yan, D.-X. Xiao, J. Kang, D.-Z. Yang, H.-X. Wu and A. Dong, *Rare Met.*, 2023, 1–17.

46 N. Tripathi and M. K. Goshisht, *ACS Appl. Bio Mater.*, 2022, **5**, 1391–1463.

47 E. M. Mateo and M. Jiménez, *Antibiotics*, 2022, **11**, 1205.

48 A. Chahardoli, F. Qalekhani, Y. Shokoohinia and A. Fattahi, *Bull. Mater. Sci.*, 2022, **45**, 88.

49 D. Wei, Y. Yu, X. Zhang, Y. Wang, H. Chen, Y. Zhao, F. Wang, G. Rong, W. Wang and X. Kang, *ACS Nano*, 2020, **14**, 16984–16996.

50 H. Wang, Z. Xu, Q. Li and J. Wu, *Eng. Regen.*, 2021, **2**, 137–153.

51 P. Dam, M. Celik, M. Ustun, S. Saha, C. Saha, E. A. Kacar, S. Kugu, E. N. Karagulle, S. Tasoglu and F. Buyukserin, *RSC Adv.*, 2023, **13**, 21345–21364.